Journal of Materials Chemistry C

ROYAL SOCIETY OF CHEMISTRY

PAPER

View Article Online
View Journal

Cite this: DOI: 10.1039/d6tc00764c

A superhydrophobic bilayer anisotropic conductive film with improved reliability for electronic interconnects

Wei Zhao,[ab] Guoxiang Zhang,[ab] Peipei Li,*[ab] Libo He,[c] Wenfeng Zhu,[d] Lei Li,[d] Houbu Li,[d] Qi Zhang,[e] Zhanchen Guo*[a] and Xiaowei Liu *[f]

Anisotropic conductive films (ACFs) are essential interconnect materials in flexible, high-density electronics but suffer from low functional reliability under humid or contaminated conditions. A superhydrophobic bilayer ACF (S-ACF) is developed to address this limitation through a scalable spray-coating process that deposits a composite of vapor-phase SiO_2 nanoparticles and styrene–ethylene–butylene–styrene (SEBS) onto a conventional epoxy-based ACF. The resulting film exhibits a dual-layer architecture in which the SiO_2/SEBS topcoat forms a micro–nano hierarchical texture with low surface energy, yielding a static water contact angle of 150° compared to 64° for the pristine ACF. Despite the surface modification, the bonding strength (17.1 MPa) and *Z*-axis contact resistance (1.64 Ω) remained nearly identical to those of the unmodified counterpart (17.2 MPa, 1.58 Ω). Additionally, the minimum lateral insulation distance of the S-ACF was approximately 60 μm, confirming that both the mechanical and electrical integrity were preserved. The superhydrophobic surface endures over 200 abrasion and tape-peel cycles while retaining ≥145° contact angle and exhibits a twofold reliability enhancement in humid-heat stability (85 °C/85% RH, resistance inflection shifted from ~150 to ~300 hours). The design in this work offers a practical route toward durable, moisture-resistant interconnects for next-generation flexible electronics.

Received 10th March 2026,
Accepted 1st May 2026

DOI: 10.1039/d6tc00764c

rsc.li/materials-c

1. Introduction

Electronic components are rapidly evolving toward greater integration, flexibility, and miniaturization, driven by emerging applications ranging from drones[1–3] and high-resolution displays,[4–6] to implantable medical devices,[7–9] robotic electronic skin,[10,11] and flexible human–machine interfaces.[12–15] The role of electronic packaging in modern electronic systems has become increasingly critical. Among various interconnection approaches, flip-chip bonding has emerged as a mainstream technology for high-density, fine-pitch packaging owing to its reduced interconnect pitch and streamlined processing. In current flip-chip assembly, interconnect materials are predominantly metallic solders, with conventional Sn–Pb solder being a representative example.[16,17] However, flip chip bonding using metallic solders can only achieve a minimum bonding interconnect pitch of several hundred micrometers, making it difficult to meet the demands for high density and flexibility in device development.[18,19] Consequently, developing novel bonding interconnect materials has become an imperative requirement to overcome this challenge.

Anisotropic conductive film (ACF) serves as a key interconnect medium that provides out-of-plane (*z*-axis) electrical conduction while ensuring robust mechanical adhesion.[20–22] Structurally, ACFs are polymer–particle composites comprising conductive microspheres (MPs) dispersed in an insulating matrix (*e.g.*, epoxy or acrylic resins).[23–25] During hot-pressing, the MPs are compressed to form vertical conductive paths between opposing contact pads, while the cured adhesive maintains the deformed state of the conductive particles and ensures stable electrical contact with the mating electrodes, simultaneously preserving lateral insulation. This synergy of particle architecture and

[a] Shaanxi Key Laboratory of High-Orbits-Electron Materials and Protection Technology for Aerospace, School of Advanced Materials and Nanotechnology, Xidian University, Xi'an, Shaanxi, 710071, P.R. China. E-mail: lip@xidian.edu.cn, guozhanchen@xidian.edu.cn
[b] State Key Laboratory of Electromechanical Integrated Manufacturing of High-performance Electronic Equipments, Xidian University, Xi'an, Shaanxi, 710071, P.R. China
[c] Shanghai Aerospace Resin based Composite Engineering Technology & Research Center, Shanghai Composites Science & Technology Co., Ltd., Shanghai, 201112, P.R. China
[d] Tubular Goods Research Institute, China National Petroleum Corporation & State Key Laboratory of Oil and Gas Equipment, Xi'an, Shaanxi, 710065, P.R. China
[e] Zhengzhou Tobacco Research Institute, China National Tobacco Corporation, Zhengzhou, Henan, 450001, P.R. China
[f] Division of Physical Science and Engineering, King Abdullah University of Science and Technology, Thuwal 23955-6900, Kingdom of Saudi Arabia. E-mail: xiaowei.liu@kaust.edu.sa

cross-linked polymer networks results in robust interfacial adhesion and toughness across diverse substrates, meeting the stringent requirements of low contact resistance and mechanical reliability of fine-pitch assemblies. To further enhance electrical performance of ACFs, recent efforts have focused on optimizing particle arrangement and composition. For instance, Cao *et al.* used transient emulsion self-assembly and nanosecond-laser processing to rapidly fabricate pure-Au microsphere arrays within photolithographic templates, creating arrayed ACFs with stable conduction under deep-press conditions.[26] Park *et al.* employed UV soft-template patterning and frictional alignment to precisely position Au-coated PS microspheres in an elastomeric matrix, producing ordered, stretchable ACFs resistant to particle migration.[27] Similarly, Hao *et al.* introduced a polyaniline (PANI) intermediate layer to streamline Ag plating on polystyrene (PS) beads, forming PS@PANI@Ag microspheres; through template-friction assembly, they fabricated arrayed ACFs that achieved a low interconnection of 1.78 Ω and retained conductivity after 120 hours of testing at 85 °C/85% RH.[28] While these advances in particle engineering, matrix optimization, and deterministic ordering significantly enhance contact formation and adhesion, they do not fundamentally address the root causes of low interface reliability. In practical environments—such as humid-heat aging, thermal cycling, and repeated bending—moisture exposure, surface contaminant accumulation, and electrochemical reactions can still trigger contact resistance drift and circuit failure. Consequently, ensuring long-term reliability under these mechanically and humid-heat conditions remains a challenge for ACF-based interconnect technologies.

Among the available strategies to improve environmental and interfacial reliability, superhydrophobic coatings with micro–nano hierarchical textures offer a compelling solution by blocking moisture ingress, suppressing electrochemical corrosion, and minimizing residue accumulation.[29–33] These surfaces combine large static contact angles with small roll-off angles, imparting anti-fouling and self-cleaning properties. Their multiscale architectures trap air pockets that reduce the effective solid–liquid contact area and surface free energy, enabling droplets to detach rapidly in a ''ball-like'' fashion and providing durable protection under harsh conditions. Representative studies demonstrate their robustness. Wang *et al.* densely embedded near-zero-shrinkage superhydrophobic silica aerogels into rigid Fe–Ni foams with regular dodecahedral units, followed by fluorination.[34] The obtained interpenetrating composite sustained ~7.4 MPa compressive strength at 8% strain, exhibited minimal wear (≈0.567 mm^3) after 5000 abrasion cycles, and maintained performance under extreme temperature, humidity, pressure, and abrasion. In a flexible context, Zhang *et al.* developed superhydrophobic and highly stretchable films by blending vulcanized natural latex with a silicone emulsion, followed by surface modification; these films preserved superhydrophobicity at 500% tensile strain and maintained water contact angles above 155° after 300 cycles at 300% strain.[35] Collectively, these studies demonstrate that robust hydrophobic barriers can remain functionality under coupled mechanical and environmental stressors.

Building on these advances, we developed a superhydrophobic bilayer anisotropic conductive film (S-ACF) by applying a conformal SiO_2@SEBS nanocomposite topcoat to an original ACF. This top layer confers stable water repellency, elevating the water contact angle from 64° to 150°, which effectively suppresses moisture absorption and surface contamination. SEBS was selected as the binder for the superhydrophobic coating because it offers good processability, flexibility, and cyclohexane solubility, enabling uniform spray coating. In addition, its fluorine-free nature makes it relatively environmentally friendly and suitable for practical electronic packaging application. Notably, the bilayer configuration retains the core mechanical and electrical performance of the base ACF, with negligible change in lap-shear strength (17.2 → 17.1 MPa) and *z*-axis resistance (1.58 → 1.64 Ω). Most importantly, under 85 °C/85% RH testing, the onset of resistance rise is delayed from 150 to 300 hours, indicating a twofold enhancement in operational lifetime against moisture-induced failure. In addition, peel-resistance and abrasion tests were conducted, during which the cured S-ACF maintained a water contact angle of ≥145° even after 200 test cycles, indicating excellent mechanical robustness of the superhydrophobic surface. Overall, this work introduces a simple, scalable, and materials-compatible strategy to countering key failure of low reliability under humid or contaminated conditions in ACFs, paving the way for durable, fine-pitch interconnects in flexible electronics and wearable systems.

2. Experimental

2.1 Materials

Hydrochloric acid (HCl, 37%), aqueous ammonia ($NH_3{\cdot}H_2O$, 25–28%), Ethyl alcohol (C_2H_5OH, Analytical Reagent), cyclohexane (C_6H_{12}, Analytical Reagent) and tetrahydrofuran (THF) were obtained from Sinopharm Chemical Reagent Co., Ltd. Silver nitrate ($AgNO_3$, Analytical Reagent), glucose ($C_6H_{12}O_6$, Analytical Reagent), potassium sodium tartrate ($NaKC_4H_4O_6$, Analytical Reagent), tin(II) chloride dihydrate ($SnCl_2{\cdot}2H_2O$, Analytical Reagent), 3-glycidoxypropyltrimethoxysilane (KH560) were provided by Shanghai Macklin Biochemical Co., Ltd. Silica (SiO_2, 10 μm) was supplied by Orite New Materials. Fumed silica was provided by Hubei Huifu Nano Materials Co., Ltd. Thermoplastic polyurethane (TPU) was provided by Yuanding Plastics Co., Ltd. Styrene ethylene butylene styrene (SEBS) was provided by Shangsu Technology Co., Ltd. Epoxy resin (E51) was provided by Shanghai Macklin Biochemical Technology Co., Ltd. The curing agent (Latent, HS-604) was provided by Chuzhou Huisheng Electronic Materials Co., Ltd. All chemicals were used as received, without further purification.

2.2 Preparation of the SiO_2@Ag conductive fillers

The SiO_2@Ag conductive fillers were synthesized *via* an electroless plating method. Briefly, SiO_2 particles were dispersed in ethanol to form an uniform suspension. The particles were sensitized by adding a solution of $SnCl_2{\cdot}2H_2O$ in hydrochloric

acid, followed by magnetic stirring and filtration to obtain Sn^{2+}-adsorbed silica. Separately, a silver ammonia solution was prepared by adding ammonia dropwise to an aqueous $AgNO_3$ solution until the initial precipitate dissolved. The sensitized SiO_2 particles were then introduced into the silver ammonia solution under stirring. Subsequently, an aqueous mixture of glucose and potassium sodium tartrate was added dropwise as a reducing agent, leading to the deposition of silver nanoparticles onto the SiO_2 surfaces, as indicated by a color change to black. The resulting SiO_2@Ag nanoparticles were isolated by repeated washing with deionized water and dried thoroughly.[36]

2.3 Preparation of the superhydrophobic bilayer anisotropic conductive film (S-ACF)

The superhydrophobic bilayer anisotropic conductive film (S-ACF) was fabricated by spray-coating a hydrophobic top layer onto a pre-stretched base ACF. First, the epoxy resin and TPU were first thoroughly mixed at a mass ratio of 1 : 1 and dispersed in tetrahydrofuran. Subsequently, SiO_2@Ag conductive particles and a latent curing agent were added. The original ACF was prepared by doctor-blading a mixture of epoxy resin, curing agent, and SiO_2@Ag conductive filler (mass ratio = 10 : 8 : 7) in solvent onto a PTFE film.[36] Under the formulation used in this work, the volume fraction of SiO_2@Ag conductive fillers in the adhesive matrix is estimated to be ~8–9 vol%, based on typical densities of the epoxy matrix (~1.2 g cm^{-3}) and SiO_2@Ag core–shell particles (~5.0 g cm^{-3}). A blade gap of 150 μm and a coating speed of 10 mm s^{-1} were used, followed by lamination with a release liner. The ACF was then uniaxially stretched to 150% of its original length and fixed in position. Prior to spray-coating, the ACF was stretched to expose surface grooves and valleys on the originally non-smooth ACF surface, which facilitates more uniform coverage of the superhydrophobic layer. The hydrophobic coating solution was formulated by dissolving vapor-phase SiO_2 in cyclohexane, followed by sonication and stirring, after which SEBS was added. This SiO_2/SEBS solution was sprayed onto the stretched ACF using a spray gun at a pressure of 0.2 MPa, a distance of 10–15 cm, and a traverse speed of approximately 5 cm s^{-1}. After complete solvent evaporation, the film was released to recover its original dimensions, yielding the final S-ACF with a conformal superhydrophobic surface.

2.4 Measurements

The surface morphology of samples was characterized using a scanning electron microscope (SEM, Hitachi SU8600). Surface topography and roughness were analyzed with a laser scanning confocal microscope (LSCM, Olympus LEXT OLS5100). The crystal structures of the pristine ACF, superhydrophobic bilayer ACF, fumed silica, and SiO_2 microspheres were determined by X-ray diffraction (XRD, Bruker D8 Advance), while Fourier transform infrared spectroscopy (FTIR, Thermo Scientific) identified chemical functional groups. Static water contact angles were measured using an optical goniometer (Biolin Scientific TFL400) with 4 μL droplets of deionized water dispensed from a height of 1 cm. A high-speed camera (YVSION OSG030-815UCTZ, 300 fps) captured the dynamic droplet-surface interactions during contact-angle measurement. Abrasion resistance was evaluated by sliding a 100 g weight attached to the sample across a 10 cm path on 2000-grit sandpaper, where one back-and-forth motion was counted as one cycle. Peel resistance was tested by adhering 3M 810 tape to the surface, pressing with a 200 g weight, and subsequently peeling it off. Stain resistance was assessed by immersing samples in a red ink aqueous solution for 1 minute. Bonding strength were analyzed according to the GB/T 7124-2008 standard using a universal testing machine (ZM-30000N).[37] Copper tape specimens (40 mm × 10 mm × 0.3 mm) with an overlap area of 10 mm × 5 mm was cured at 150 °C for 60 minutes, and tested at a loading rate of 10 mm min^{-1}. Tensile strength and elongation at break were measured per GB/T 2567-2008 at the same loading rate.[38] For all mechanical tests, five parallel samples were assessed, and results are reported as the mean ± standard deviation. Using two pieces of 40 mm × 10 mm × 0.3 mm copper sheets, sandwiching 10 mm × 5 mm S-ACF in the middle, hot pressing for 10 minutes under 0.3 MPa and 150 °C conditions, and then curing for one hour at 150 °C, the bonding test sample can be prepared. Cut the S-ACF into a 10 mm × 50 mm rectangle and cure it at 150 °C for one hour to obtain the tensile test sample. Specific test diagrams are shown in Fig. S1 and S2. Electrical properties were evaluated using a test structure composed of an ACF layer hot-pressed between two polyimide (PI) films with patterned silver electrodes. Bonding tests were carried out at 150 °C under a pressure of 0.3 MPa for 10 min using Ag electrodes patterned on PI films with a fixed electrode spacing of 1 mm. The bonded assembly was then fully cured at 150 °C for 1 h, after which the electrical properties were measured directly using a standard ohmmeter: the resistance between the top and bottom electrodes was used to evaluate *Z*-axis electrical conduction, while the resistance between laterally separated electrodes was used to assess *X*–*Y* directional electrical insulation. The specific contact resistance test schematic is shown in Fig. S3. Unless otherwise stated, all ACF and S-ACF samples were fully cured prior to any characterization. All wettability, surface morphology, mechanical, and electrical measurements reported in this work were conducted on cured samples.

3. Results and discussion

3.1. Preparation and characterization of S-ACF

The base ACF was first synthesized on a release film *via* a tape-casting process. As shown in Fig. 1a, this original ACF consisted of silver-coated SiO_2 microspheres as conductive fillers dispersed in an epoxy resin matrix with a latent curing agent. The epoxy resin and TPU were first thoroughly mixed at a mass ratio of 1 : 1 and dispersed in tetrahydrofuran. Subsequently, SiO_2@Ag conductive particles and a latent curing agent were added. The original ACF was prepared by doctor-blading a mixture of epoxy resin, curing agent, and SiO_2@Ag conductive filler (mass ratio = 10 : 8 : 7) in solvent onto a PTFE film.[36] The silver-coated SiO_2 spheres were synthesized in-house, and their successful formation was verified by X-ray diffraction (XRD) and scanning electron microscopy (SEM). The XRD pattern (Fig. S4a)

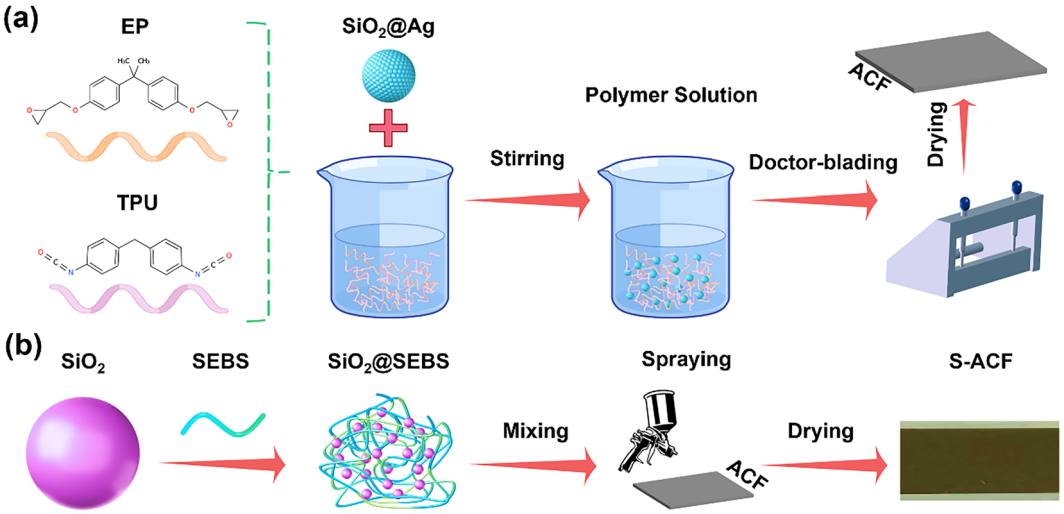

Fig. 1 Schematic illustration of the fabrication process for (a) the base ACF and (b) the superhydrophobic bilayer anisotropic conductive film (S-ACF).

of pristine SiO_2 shows a broad diffraction peak at ~20°, confirming its amorphous structure. Following silver coating, distinct peaks at 38.1°, 44.3°, 64.4°, and 77.4° emerged, corresponding to the (111), (200), (220), and (311) planes of face-centered cubic silver, respectively, consistent with standard reference data. SEM images (Fig. S4b and c) provide complementary morphological evidence: the pristine SiO_2 spheres are smooth and uniform, whereas the silver-coated spheres maintain their spherical shape but exhibit a roughened surface covered with granular features, which are attributed to Ag nanoparticles deposited on the SiO_2 surface rather than a continuous coating layer. These nanograins are attributed to metallic Ag crystallites, confirming successful silver layer deposition. To construct the superhydrophobic bilayer, the ACF surface was finally spray-coated with a cyclohexane solution containing vapor-phase SiO_2 nanoparticles and SEBS. Upon solvent evaporation, a conformal topcoat with micro–nano-scale roughness and intrinsically low surface energy was formed, completing the S-ACF structure, as illustrated in Fig. 1b.

The surface of the unmodified ACF appears relatively smooth and compact. As shown in the SEM image (Fig. 2a), only shallow grooves and slight undulations are visible, which likely arise from epoxy curing shrinkage. This morphology lacks the hierarchical micro–nano-scale roughness required to induce superhydrophobicity. In contrast, the SiO_2/SEBS-modified surface (Fig. 2b) reveals a densely packed coating of micro–nano-structured particles, forming a highly rough and porous texture favorable for water repellence.[39,40] The three-dimensional profile obtained by laser scanning confocal microscopy (LSCM, Fig. 2c) shows a continuous hierarchical topology composed of nano-steps and protrusions, with an arithmetic average roughness (Sa) of approximately 1.82 μm and a root mean square height (Sq) of approximately 2.48 μm. Such engineered

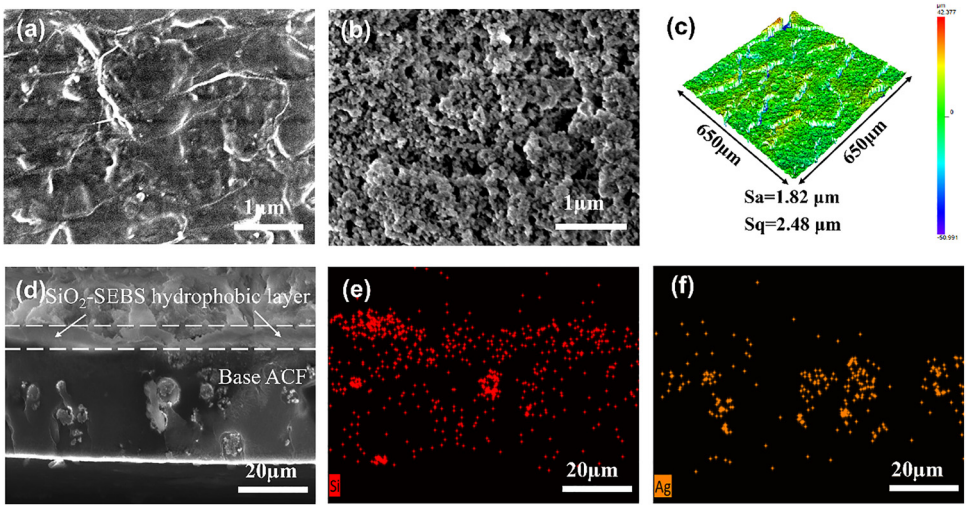

Fig. 2 Morphological and elemental characterization of cured ACF and S-ACF. (a) and (b) Top-surface SEM images of (a) ACF and (b) S-ACF. (c) LSCM image of the S-ACF surface. (d) Cross-sectional SEM image revealing the internal structure of S-ACF. (e) and (f) Corresponding EDS elemental maps of the S-ACF cross-section.

roughness is critical for superhydrophobicity, as the hierarchical structures trap a stable layer of air within their cavities, generating a gas film at the liquid–solid interface. This air film acts as a physical barrier, preventing direct contact between water and the ACF surface, thereby significantly enhancing its corrosion resistance. Simultaneously, the inherent low surface energy of the vapor-phase SiO_2 further reduces interfacial free energy. The synergistic effect of surface roughness and low energy minimizes the solid–liquid contact area, leading to nearly spherical water droplets characterized by a high contact angle and robust hydrophobicity behavior.

Cross-sectional analysis of the S-ACF provides further insight into its structure. The SEM image (Fig. 2d) reveals a distinct, continuous SiO_2/SEBS top layer that forms a clear interface with the underlying ACF. This topcoat adheres tightly to the epoxy matrix without delamination or voids and exhibits internal protrusions consistent with the micro–nano-scale roughness observed on the surface. Such a bilayer architecture underpins the material's dual functionality. The dense, rough top layer confers superhydrophobicity and antifouling capability, while its thinness and elasticity—attributed to the SEBS elastomer—ensure that it does not impede the penetration of conductive particles during hot-pressing. As a result, reliable *z*-axis conductive pathways are maintained, preserving the ACF's anisotropic conductivity, as corroborated by subsequent electrical characterization. Elemental mapping *via* EDS further verifies this stratified design: the Si distribution (Fig. 2e) is concentrated in the surface region, confirming the enrichment of vapor-phase SiO_2 nanoparticles, where the isolated Si signals within the ACF bulk originate from Ag-coated SiO_2 fillers. Conversely, the Ag signal (Fig. 2f) is predominantly localized at these filler sites within the conductive layer, illustrating that the current-carrying network remains intact beneath the hydrophobic shield. This clearly defined "hydrophobic-conductive" dual-layer structure provides the structural basis for achieving hydrophobicity.

3.2. Hydrophobic and mechanical properties of S-ACF

To further validate the successful construction of the S-ACF bilayer, we performed X-ray diffraction (XRD) and Fourier-transform infrared (FTIR) spectroscopy (Fig. 3a and b). In the XRD patterns (Fig. 3a), the diffraction peaks corresponding to the Ag-coated SiO_2 fillers remain identical to those discussed above, indicating that their crystalline structure as conductive components within the ACF matrix is fully preserved. After modification, an additional amorphous scattering feature near $2\theta \approx 20^\circ$ becomes evident, attributable to the SiO_2-containing top layer, further supporting the successful introduction of the hydrophobic coating. Notably, no discernible peak shift or broadening is observed, indicating that the modification does not introduce measurable lattice distortion or micro strain in the Ag fillers. The retention of both peak intensity and sharpness implies that the hydrophobic SiO_2/SEBS overlayer is thin and exerts negligible influence on the diffraction from the underlying conductive network, aligning with the intended bilayer design in which electrical pathways through Ag are maintained. FTIR spectra (Fig. 3b) provide complementary evidence for this bilayer configuration. The SiO_2@SEBS coating exhibits a C–H stretching band from SEBS near 2900 cm^{-1} and a pronounced Si–O absorption centered around 1100 cm^{-1}, dominated by Si–O–Si asymmetric stretching characteristic of vapor-phase SiO_2. Compared with the unmodified ACF, the S-ACF spectrum shows a markedly enhanced C–H stretching signal ($\sim$2900 cm^{-1}), indicating the presence of the organic SEBS component, and

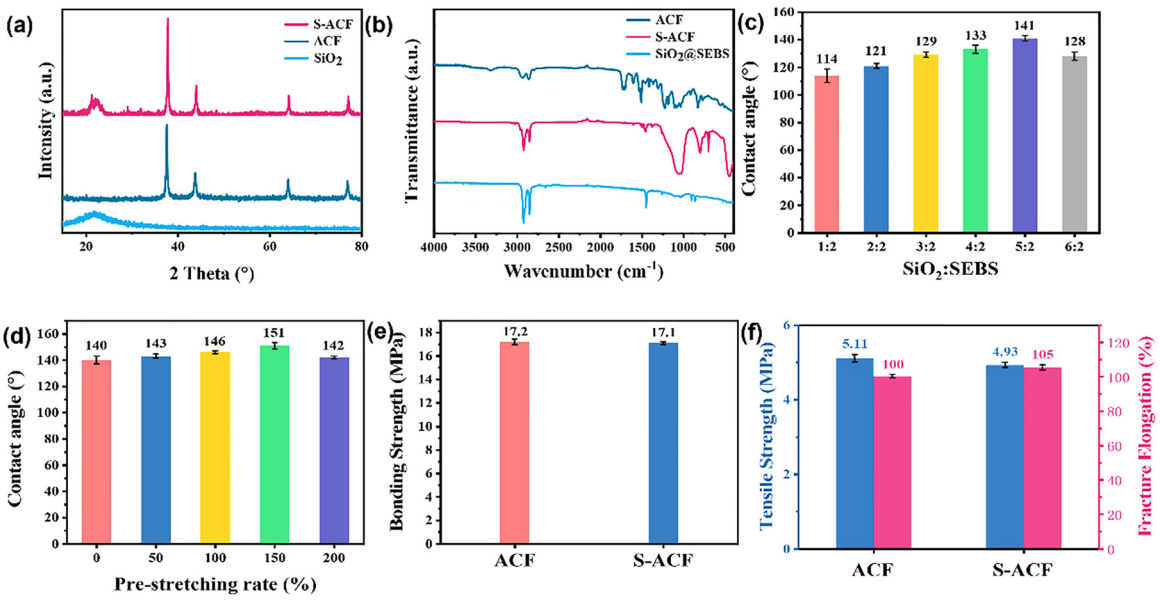

Fig. 3 Structural and mechanical characterization of the ACF and S-ACF. (a) XRD patterns of ACF, SiO_2, and S-ACF, identifying crystalline phases. (b) FTIR spectra of ACF, a SiO_2/SEBS mixture, and S-ACF, confirming chemical functionalization. (c) Water contact angle of S-ACF plotted against increasing SiO_2 filler content. (d) Water contact angle of S-ACF measured under 0–200% pre-stretching rate. (e) Bonding strength of the S-ACF. (f) Tensile strength and elongation at break for ACF and S-ACF, comparing their mechanical performance.

an intensified Si–O band ($\sim$1100 cm^{-1}), reflecting the enrichment of SiO_2 at the outer surface following cyclohexane evaporation during modification. Together, the XRD and FTIR results consistently demonstrate the successful deposition of a SiO_2-containing hydrophobic overlayer on the ACF while preserving the crystalline integrity and electrical continuity of the Ag-based conductive network. This confirms that the surface modification imparts hydrophobic functionality with minimal impact on the film's electrical performance.

In practical applications, the service life of ACFs is often curtailed by ambient humidity and condensate, as moisture adsorption and penetration can gradually degrade the polymer matrix and interfacial electrical contacts, leading to increased contact resistance and reduced reliability. Motivated by the "water-beading" effect of waterproof textiles and prior work by Wang *et al.*, we implemented a hydrophobic surface modification to improve environmental stability.[41] We first quantified the effect of vapor-phase SiO_2 loading on hydrophobicity (Table S1). With SEBS (200 mg) and cyclohexane (100 mL) kept constant, the SiO_2 dose was varied from 100 to 600 mg (SiO_2 : SEBS = 1 : 2 to 6 : 2). As shown in Fig. 3c, the static contact angle rose monotonically with SiO_2 content, peaking at the 5 : 2 formulation (#8 in Table S1, SiO_2 = 500 mg) from $\sim$114° to 141°. Beyond this point, the contact angle declined to $\sim$128° at 6 : 2. This "rise-then-fall" trend suggests that, moderate particle loadings enable the formation of continuous micro/nano hierarchical roughness that stabilizes an air cushion, whereas excessive SiO_2 induces local agglomeration, disrupts roughness uniformity, and compromises air-pocket continuity which diminishes hydrophobicity. Consistently, the unmodified ACF shows groove-rich, scale-mismatched topography, limiting its intrinsic water repellence. It should be noted that the water contact angle measurements were performed after complete curing of the ACF, ensuring that the measured wettability reflects the intrinsic surface state of the cured material.

Building on this insight, we employed a pre-stretching-assisted spray method to amplify the surface structure. Leveraging the ductility of the epoxy/TPU matrix prior to full cure, the ACF was axially pre-stretched by 50%–200% before SiO_2@SEBS deposition. As summarized in Fig. 3d, the contact angle exhibits a non-monotonic dependence on pre-strain: it increases with strain, reaching 150° (superhydrophobic regime) at 150% pre-stretching process, and slightly declines at 200%. We attribute the optimum to strain-mediated "opening" and magnification of surface grooves, which improves coating conformity and fosters favorable micro/nano composite roughness. This interpretation is further supported by the LSCM comparison of the resulting S-ACF surfaces prepared with and without pre-stretching (Fig. S5), where the pre-stretched sample exhibits more pronounced groove features and higher areal roughness parameters (Sa and Sq). Over-stretching likely perturbs feature uniformity and/or introduces local defects, weakening the Cassie state. Together, composition tuning (SiO_2 : SEBS = 5 : 2) and moderate pre-stretching process ($\sim$150%) deliver a robust superhydrophobic surface, providing an effective route to mitigate humidity-induced degradation and extend the service durability of ACFs. Fig. S6a and b illustrate the anti-soiling and self-cleaning capabilities of S-ACF, underscoring its sustained resistance to moisture and stains during operational use.

Meanwhile, we also assessed whether the superhydrophobic modification affects the bulk mechanical properties of the ACF. Fig. S7a (after the bonding test) and b (after the tensile test) show rough and torn fracture morphologies, accompanied by clear plastic deformation and tearing features. No large-scale delamination of the superhydrophobic surface layer is observed; instead, failure occurs primarily within the ACF bulk rather than at the interfaces. This indicates that interfacial adhesion exceeds the cohesive strength of the ACF, leading to crack propagation through the bulk. In addition, as shown in Fig. 3e, the bonding strengths of the modified and unmodified specimens are 17.2 MPa and 17.1 MPa, respectively—essentially identical within experimental uncertainty—indicating that the thin SiO_2@SEBS overlayer does not compromise the cohesive integrity of the adhesive network or its interfacial bonding. Specific test diagrams are shown in Fig. S1 and S2. Similarly, uniaxial tensile metrics (Fig. 3f) were largely preserved: the S-ACF exhibits an ultimate tensile strength of 4.93 MPa and an elongation at break of 105%, compared with 5.11 MPa and 100% for the pristine ACF. The near invariance of both strength and ductility confirms that the hydrophobic coating neither embrittles nor plasticizes the matrix. These mechanical outcomes are consistent with cross-sectional SEM imaging (Fig. 2d), which reveals an $\sim$3 μm surface layer intimately bonded to the underlying ACF without interfacial defects or delamination. Collectively, optimizing the SiO_2 volume fraction and applying the pre-stretching–assisted spray process enables the tuning of surface wettability into the superhydrophobic regime while preserving load-bearing and deformability characteristics. This strategy therefore enhances environmental durability of ACF (*e.g.*, resistance to humidity and condensate) without compromising mechanical performance.

To directly compare how each treatment alters wettability, Fig. 4 compiles static contact-angle and adhesion behaviors of the samples. Representative optical images of contact angles for the pristine ACF, the unstretched SiO_2@SEBS-modified ACF, and the pre-stretched, spray-coated S-ACF are shown in Fig. 4a–c, respectively. The unmodified ACF exhibits a modest static contact angle of 64°, while SiO_2@SEBS modification increases the angle to 141°. Incorporating the pre-stretching-spray-coating step further elevates the angle to 150°, entering the superhydrophobic regime. This progressive improvement aligns with the trend in Fig. 3d and substantiates the effectiveness of our synergistic "formulation-pre-stretching-coating" strategy. To assess surface adhesion, a high-speed camera recorded the dynamic "contact-separation" process between a 4 μL water droplet and the film surface (Fig. 4d). On the S-ACF, the droplet maintains nearly spherical upon contact and detaches cleanly during needle retraction without residue, indicating extremely weak solid–liquid interfacial adhesion and a canonical low-adhesion superhydrophobic state.

The superior hydrophobicity of the SiO_2-SEBS couple can be rationalized by examining the surface morphologies in Fig. 5. Without coating (Fig. 5a and e), the groove-rich surface lacks a percolating, multiscale texture capable of stably trapping air. Introducing vapor-phase SiO_2 alone (Fig. 5b and f) leads to

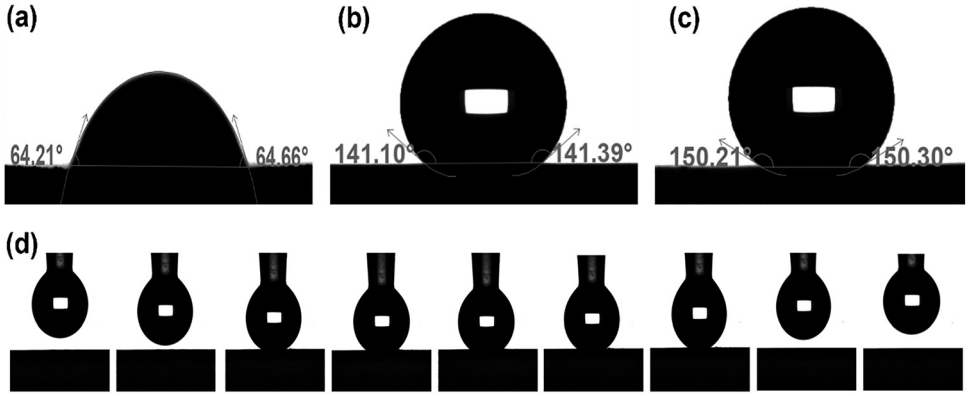

Fig. 4 Evaluation of hydrophobic and anti-fouling properties. (a)–(c) Evolution of the static water contact angle: (a) pristine ACF, (b) S-ACF, and (c) S-ACF under 150% tensile strain. (d) Dynamic self-cleaning demonstration, where water droplets are unable to adhere to the S-ACF surface and easily roll off. All contact angle measurements were carried out on fully cured ACF and S-ACF samples.

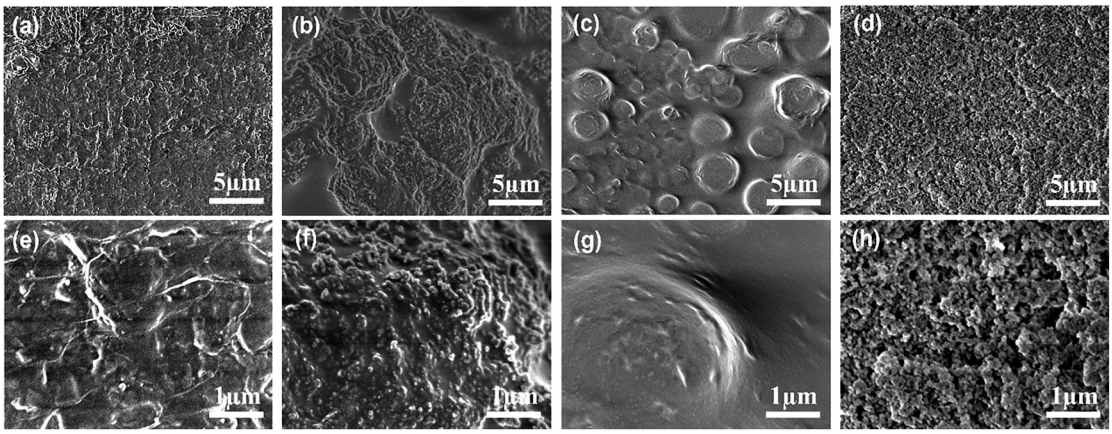

Fig. 5 Morphological evolution of the S-ACF. Representative SEM images show: (a) and (e) the pristine ACF; (b) and (f) the intermediate state after SiO_2 deposition; (c) and (g) the subsequent SEBS modification; and (d) and (h) the final S-ACF.

"cauliflower-like" agglomeration and poor dispersion; during epoxy softening/curing, these clusters are readily embedded, blunting asperities and suppressing effective micro–nano features at the interface. Applying SEBS alone (Fig. 5c and g) produces a dense, relatively smooth organic film that fills pre-existing grooves, again preventing air-cushion formation. Only when SiO_2 and SEBS act synergistically (Fig. 5d and h) does the elastomeric SEBS act as a compliant binder, immobilizing SiO_2 particles that partially protrude at the surface. SEBS also improves SiO_2 dispersion and suppresses agglomeration during spray coating, facilitating the formation of a more uniform micro-/nano-scale hierarchical roughness. In addition, SEBS provides stable anchoring sites that firmly immobilize SiO_2 within the surface layer, reducing particle pull-out and structural damage under repeated mechanical loading, and thereby enhancing the wear resistance of the superhydrophobic coating. This configuration constructs a continuous micro–nano hierarchical roughness with interconnected voids. The interparticle interstices function as air pockets, reducing the real solid–liquid contact area and stabilizing the Cassie state. Concurrently, the SEBS matrix enhances particle anchorage and wear resistance, mitigating pull-out and delamination. As a result, the surface texture – and thus the wetting state – remains stable during repeated use. This composite architecture unites high static contact angles with low adhesion (low hysteresis), delivering the desired low-adhesion superhydrophobic behavior.

3.3. Electrical and humid-heat reliability properties of S-ACF

Fig. 6a schematically illustrates the operating principle of the superhydrophobic anisotropic conductive film in this study. The S-ACF is first laminated onto the substrate and then hot-pressed at 0.3 MPa and 150 °C for 10 minutes. During pressing, the Ag-coated SiO_2 microspheres (~10 μm in diameter, Fig. S4c) readily penetrate the ultrathin superhydrophobic top layer (~3 μm thick, Fig. 2d), whose thickness is substantially smaller than the particle diameter. This geometry minimizes interference with electrical interconnection, consistent with the comparable initial contact resistances of the base ACF (1.58 Ω) and S-ACF (1.64 Ω). The test circuit is shown in Fig. S3. Fig. S8 and S9 display the surface and cross-section of the actual S-ACF after hot pressing. It can be observed that the conductive particles

penetrate the hydrophobic layer, and the hydrophobic layer does not erode the interior of the base ACF, confirming the conductive mechanism of the S-ACF. The superhydrophobic layer that remains in non-contact regions after hot-pressing provides a continuous moisture barrier, effectively suppressing aging and performance drift during operation.

To further evaluate the electrical performance, a test circuit comprising four parallel Ag traces on two PI films was assembled (Fig. 6b), with an electrode spacing of 1 mm. The S-ACF was hot-pressed at 0.3 MPa between aligned PI films (precisely matching A1–A4 with B1–B4) and subsequently cured at 150 °C for 1 h. The current–voltage (*I–V*) characteristics measured for the aligned electrode pairs exhibit stable and reproducible electrical conduction, indicating that effective electrical pathways are formed across the bonded interfaces (Fig. 6c). Compared with the direct A1–A1 reference, the aligned A1–B1 and A2–B2 electrode pairs show a consistent conductive response, reflecting the contribution of the bonded ACF layer while maintaining reliable electrical connectivity. In contrast, the misaligned A1–B2 electrodes display negligible current over the entire measurement range, demonstrating excellent electrical insulation along the in-plane (*X–Y*) direction. This pronounced electrical anisotropy confirms that conductive pathways are selectively established along the *Z* direction during hot pressing, while lateral conduction is effectively suppressed. Such behavior originates from the localized penetration of conductive particles under compression and the absence of continuous conductive pathways in the in-plane direction, ensuring effective *Z*-axis conduction together with robust *X–Y* insulation.

Fig. 7 systematically evaluates the mechanical durability and humid-heat reliability of the superhydrophobic anisotropic conductive film in comparison to the conventional base ACF. Abrasion resistance was quantified using a linear reciprocating test under a 100 g load over a 10 cm path on sandpaper. In parallel, adhesion resilience was assessed *via* a tape-peel test, in which 3M tape was uniformly applied under a 200 g weight and peeled at a constant speed. Contact angle measurements performed during these tests revealed exceptional retention of superhydrophobicity: after 200 abrasion cycles, the S-ACF maintained a static contact angle above 145°, a drop of only 5°, while the tape-peel test resulted in a further decrease of merely 3°, yielding 147° (Fig. 7a). This notable performance-reflecting negligible degradation of the micro–nano-structured hydrophobic surface–can be attributed to the viscoelastic SEBS matrix, which dissipates local shear and friction stresses at the micro-scale, as well as effectively anchors the gas-phase SiO_2 particles through an entrapment mechanism. Furthermore, the cross-linked epoxy network within the ACF matrix provides mechanical reinforcement and stabilizes the SEBS chains, thereby preventing particle dislodgement. Such mechanical robustness helps preserve the integrity of the superhydrophobic barrier. While the coating does not directly enhance the intrinsic metal-epoxy bonding or particle-pad contact formation, it can slow moisture/ion ingress and thereby indirectly mitigate degradation at these moisture-sensitive interfaces during humid-heat exposure.

Electrical aging behavior further corroborates these findings. Fig. 7b and Tables S2 and S3 illustrate the trend of contact resistance changes during long-term aging under accelerated humid heat conditions (85 °C, 85% RH). Unmodified base ACF exhibits a gradual increase in resistance followed by a sharp rise after 150 hours, indicating persistent deterioration of the conductive path. In contrast, S-ACF consistently maintained lower and more stable resistance values, showing significant changes only after 300 hours-meaning it achieved twice the reliability improvement over the base ACF in wet-heat aging tolerance. The mechanism behind this enhanced wet-heat reliability lies in the accelerated diffusion of water molecules into the ACF matrix under 85 °C/85% RH aging conditions. In unmodified ACF, water vapor permeates into the interior through pathways such

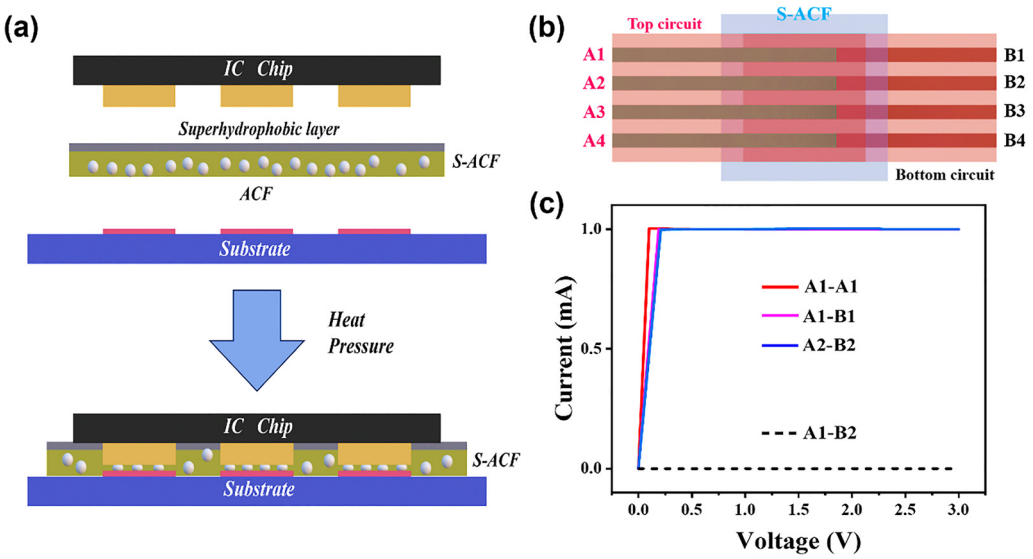

Fig. 6 Electrical conductivity of the S-ACF. (a) Schematic of conductive pathways formed after hot pressing. (b) Circuit diagram for electrical measurement with the S-ACF sandwiched between silver electrodes. (c) Linear current–voltage (*I–V*) curve confirming ohmic conduction.

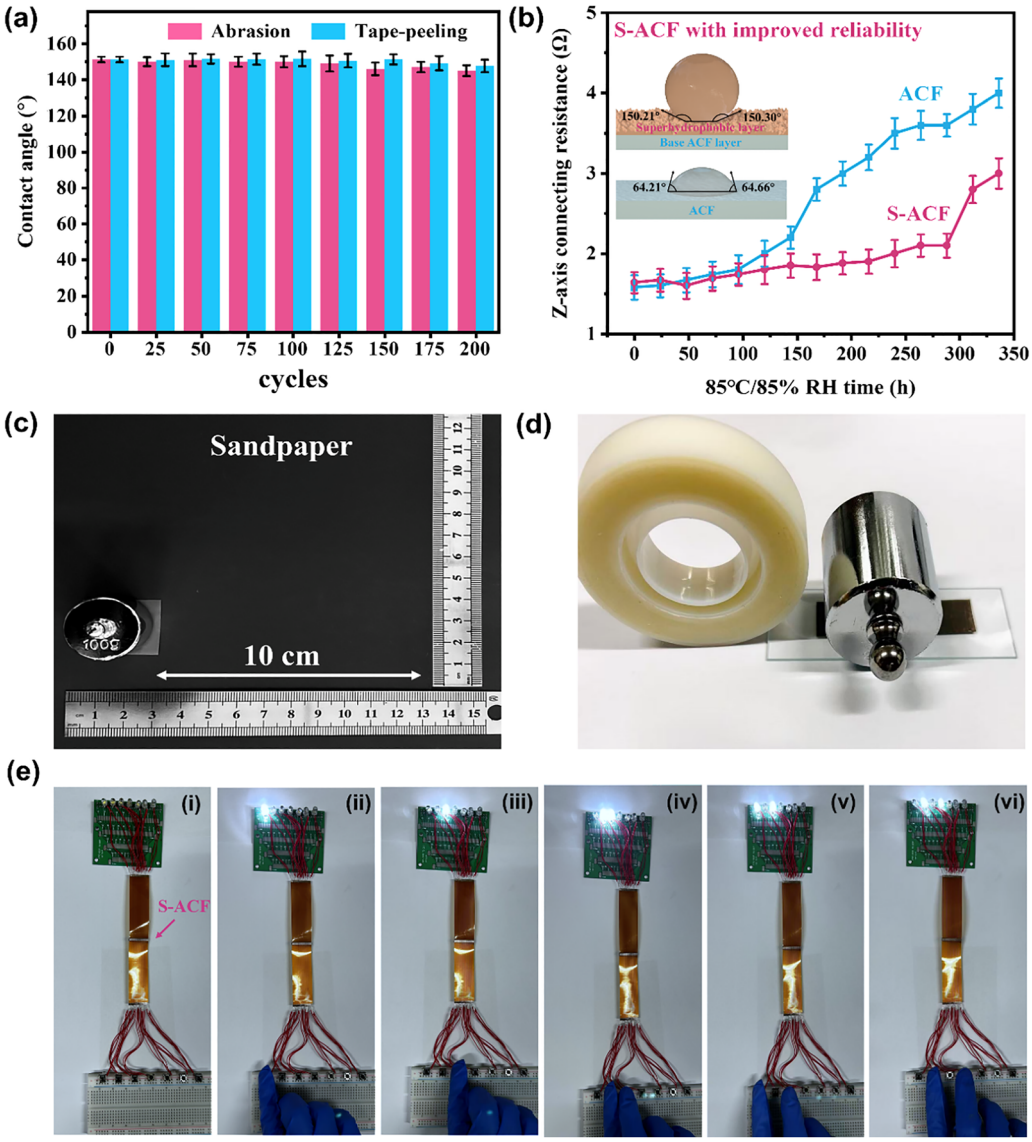

Fig. 7 Durability and humid-heat reliability of the S-ACF. (a) Evolution of the water contact angle over cycles of abrasive wear and tape peeling. (b) Performance comparison of ACF and S-ACF during an accelerated aging test at 85 °C and 85% relative humidity (RH). For the 85 °C/85% RH aging test, ten independent specimens were tested for each group. (c) Abrasion resistance test procedure, where one cycle is defined as a 10-cm linear stroke and return. (d) Adhesive tape-peeling test setup.(e) Demonstration of reliable electrical function in a circuit interconnected with S-ACF, showing device operation with various switch activations: (i) all off, (ii) switch 1, (iii) switch 3, (iv) switches 2 & 3, (v) switches 1 & 3, (vi) switches 2 & 4.

as surface micro-protrusions, interfaces, and voids, degrading electrical performance. S-ACF, however, benefits from a dense, low-energy barrier layer formed by its vapor-phase SiO_2 micro-nano structure coating. This layer obstructs vapor penetration through interfaces and voids, effectively blocking moisture ingress and delaying degradation. This inhibits the rate of resistance increase, extending the functional lifespan of electronic interconnects. From an application perspective, these durability improvements translate directly into enhanced device reliability by reducing repair frequency and extending service life under humid conditions. The bilayer S-ACF is therefore well suited for electronic interconnects exposed to moisture, condensation, or surface contamination, including foldable displays, flexible sensor arrays, outdoor flexible electronics, and compact packaging systems operating in high-humidity environments. Fig. 7c and d present the experimental photographs of the wear resistance and peel tests, respectively.

To further validate the functional anisotropy of S-ACF, a circuit assembly was constructed by connecting two FPC-200 circuit boards (each containing seven independent circuits, the spacing between different electrodes is 1 mm.) *via* the S-ACF layer. Each circuit integrates a touch switch, LED indicator (emitting white light, with LED beads measuring 3 mm in size), and 3 V power supply. As shown in Fig. 7e, pressing a specific touch switch illuminates only the corresponding LED without crosstalk or false activation. More importantly, as shown in Fig. S10a and b, we employed PI film with au interdigitated electrode as the minimal lateral insulation test circuit for the

S-ACF. Each individual electrode strip features identical line widths, with 15 electrode pairs per strip. The increased number of electrodes effectively mitigates random effects, enabling precise determination of the minimum spacing for lateral short circuits in S-ACF. Test electrodes with line widths of 50, 60, 70, 80, 90, and 100 μm between electrodes were prepared. The S-ACF was hot-pressed and cured onto the electrodes for testing. Applying a 10 V voltage between A and B electrodes revealed that only the 50 and 60 μm spacing electrodes exhibited current flow (Fig. S10b), while the 70, 80, 90, and 100 μm spacing electrodes showed no current (due to testing environment constraints, the maximum measurable current was limited to 10 mA to prevent instrument damage). This indicates that the minimum lateral insulation spacing for S-ACF is approximately 60 μm, demonstrating excellent electrical isolation and precise anisotropic conductivity.

4. Conclusions

In this study, a superhydrophobic anisotropic conductive film (S-ACF) was fabricated *via* a spray coating process employing SiO_2 and SEBS to construct a dual-layer architecture comprising a hydrophobic top layer and a conductive base. The S-ACF exhibited a static water contact angle of 150°, markedly higher than the pristine ACF (64°), thereby achieving superhydrophobicity. Mechanical integrity was fully preserved: the bonding strength remained nearly unchanged (17.1 MPa *vs.* 17.2 MPa), while tensile strength (4.93 MPa) and elongation at break (105%) were comparable to those of the unmodified ACF (5.11 MPa and 100%). Electrical performance was likewise maintained, with a *Z*-axis contact resistance of 1.64 Ω, similar to the original ACF (1.58 Ω), and minimum lateral insulation with approximately 60 μm, confirming that the thin hydrophobic layer does not hinder conductive pathways. Durability testing further highlighted the robustness of the S-ACF: after 200 cycles of abrasion and tape-peeling, the contact angle remained $\geq$145°, indicating strong retention of surface hydrophobicity. Under accelerated aging (85 °C/85% RH), the resistance inflection point shifted from ~150 h to ~300 h, demonstrating a twofold humid-heat reliability improvement in humid heat stability. Overall, this bilayer design synergistically optimizes hydrophobicity, electrical conductivity, mechanical strength, and environmental resilience, providing a practical and scalable strategy for developing high-performance ACFs in moisture-sensitive and flexible electronic applications.

Author contributions

W. Z.: methodology, investigation, data curation, writing–original draft. G. Z.: investigation, data curation. P. L.: methodology, investigation, data curation, supervision. funding acquisition, resources, project administration, writing – review & editing. L. H.: methodology, data curation. W. Z.: investigation, data curation. L. L.: resources. H. L.: resources. Q. Z.: resources. Z. G.: resources, writing – review & editing. X. L.: resources, project administration, writing – review & editing. Fig. 1 by figdraw.com

Conflicts of interest

The authors declare no conflict of interest.

Data availability

The data supporting this article have been included as part of the supplementary information (SI). Supplementary information is available. See DOI: https://doi.org/10.1039/d6tc00764c.

Acknowledgements

This work was financially supported by the National Natural Science Foundation of China (No. 22575181 and No. 22404130). The authors also acknowledge the Fundamental Research Funds for the Central Universities (No. ZYTS25238), Xidian University Specially Funded Project for Interdisciplinary Exploration (No. TZJH2024042), the Postgraduate Innovation Fund of Xidian University (No. YJSJ26019), and the support from King Abdullah University of Science and Technology.

References

1 S. Sadeghi, R. B. Canty, N. Mukhin, J. Xu, F. Delgado-Licona and M. Abolhasani, Engineering a sustainable future: Harnessing automation, robotics, and artificial intelligence with self-driving laboratories, *ACS Sustainable Chem. Eng.*, 2024, **12**, 12695–12707.
2 J. Jiang, H. Gu, R. Xu, J. Zhou, Y. Gao, L. Zhang, X. Cong, Y. Jiang and L. Song, Deep Learning-Assisted 3D Pressure Sensors for Control of Unmanned Aerial Vehicles, *ACS Appl. Mater. Interfaces*, 2025, **17**, 31107–31117.
3 Z. Wang, K. Wang, Y. Liu, X. Guan, Z. Pan, Y. Yao and T. Li, Triboelectric Sensor with a Hierarchical Structure for Omnidirectional Adaptive Wind Speed and Wind Direction Sensing for Unmanned Aerial Vehicles, *ACS Appl. Mater. Interfaces*, 2025, **17**, 23984–23995.
4 J. E. Ryu, S. Park, Y. Park, S. W. Ryu, K. Hwang and H. W. J. A. M. Jang, Technological breakthroughs in chip fabrication, transfer, and color conversion for high-performance micro-LED displays, *Adv. Mater.*, 2023, **35**, 2204947.
5 S. K. Paral, J.-Y. Jeng, C.-H. Wu, G.-W. Lin, Y.-L. Cheng and D.-Z. J. A. S. S. Lin, Nanoscale roughness to mitigate polydimethylsiloxane (PDMS) sticking in liquid crystal display (LCD) vat photopolymerization (VPP): Separation force reduction without losing resolution, *Appl. Surf. Sci.*, 2025, **683**, 161773.
6 K. M. Lee, N. Kim, J. K. Lee, H. J. Lee, S. Y. Kim and T. G. J. A. S. S. Kim, Mesh-patterned IZO/Hf-doped IGZO thin film transistors with high mobility and mechanical stability for flexible display, *Appl. Surf. Sci.*, 2025, **686**, 162102.

7 P. Jastrzebska-Perfect, G. D. Spyropoulos, C. Cea, Z. Zhao, O. J. Rauhala, A. Viswanathan and D. Khodagholy, Mixed-conducting particulate composites for soft electronics, *Sci. Adv.*, 2020, **6**, eaaz6767.

8 C. Xu, S. Guan, H. Zhang, W. Fan, X. Zhuang and X. Dong, Hierarchical hybrid crosslinking multifunctional gelatin-based hydrogel: ideal platforms for flexible wearable devices, brain–computer interfaces and biomedical applications, *J. Mater. Chem. A*, 2025, **13**, 450–459.

9 D. H. Choi, H. T. Kim, Y. Kim, K. Park, M. S. Kim, J. H. Lee, G. I. Kim, J. J. Chung and H. J. Kim, Nature-derived, biocompatible silibinin based bioresorbable neuromorphic device for implantable medical electronics, *Appl. Surf. Sci.*, 2023, **621**, 156814.

10 D. Ge, H.-Y. Yu, Z. Miao, X. He and S. Y. H. Abdalkarim, Intrinsically conductive bifunctional nanocellulose-reinforced robust and self-healable electronic skin: deep insights into multiple bonding network, property reinforcement, and sensing mechanism, ACS Sustain, *Chem. Eng.*, 2022, **11**, 1157–1167.

11 L. Chen, Y. Xu, Y. Liu, J. Wang, J. Chen, X. Chang and Y. Zhu, Flexible and transparent electronic skin sensor with sensing capabilities for pressure, temperature, and humidity, *ACS Appl. Mater. Interfaces*, 2023, **15**, 24923–24932.

12 T. Chen, P. Wei, G. Chen, H. Liu, I. T. Mugaanire, K. Hou and M. Zhu, Heterogeneous structured tough conductive gel fibres for stable and high-performance wearable strain sensors, *J. Mater. Chem. A*, 2021, **9**, 12265–12275.

13 H. R. Ansari, A. Mirzaei, H. Shokrollahi, R. Kumar, J.-Y. Kim, H. W. Kim, M. Kumar and S. S. Kim, Flexible/wearable resistive gas sensors based on 2D materials, *J. Mater. Chem. C*, 2023, **11**, 6528–6549.

14 X. Jiang, Y. Cheng, L. Shi, J. Sun and R. Wang, A soft, fatigue-free, and self-healable ionic elastomer *via* the synergy of skin-like assembly and Bouligand structure, *Angew. Chem., Int. Ed.*, 2024, **63**, e202411418.

15 W. Hong, X. Guo, T. Zhang, S. Mu, F. Wu, Z. Yan, H. Zhang, X. Li, A. Zhang and J. Wang, Flexible strain sensor based on nickel microparticles/carbon black microspheres/polydimethylsiloxane conductive composites for human motion detection, *ACS Appl. Mater. Interfaces*, 2024, **16**, 32702–32712.

16 J. Li, Y. Duan, H. Cao, Y. Wang, X. Lu, Y. Xu, R. Sun and Y. Hu, Pressure-adaptive core–shell liquid metal microspheres for reliable flip-chip interconnects, *Chem. Eng. J.*, 2025, **520**, 165694.

17 C.-K. Huang, C.-Y. Chiu, T.-L. Lai, C. Cheng, W.-H. Lai, P.-J. Chang, J.-L. Wu, C.-H. Chiang, C.-G. Wu and C.-Y. Liu, Flip-chip packaged perovskite solar cells, *Energy Technol.*, 2021, **9**, 2001129.

18 S. Jiang, X. Liu, J. Liu, D. Ye, Y. Duan, K. Li, Z. Yin and Y. Huang, Flexible metamaterial electronics, *Adv. Mater.*, 2022, **34**, 2200070.

19 J. H. Lee, K. Cho and J. K. Kim, Age of flexible electronics: emerging trends in soft multifunctional sensors, *Adv. Mater.*, 2024, **36**, 2310505.

20 H. Hwang, M. Kong, K. Kim, D. Park, S. Lee, S. Park, H.-J. Song and U. Jeong, Stretchable anisotropic conductive film (S-ACF) for electrical interfacing in high-resolution stretchable circuits, *Sci. Adv.*, 2021, **7**, eabh0171.

21 Y. Liu, Y. Pan, Z. Zheng, H. Zhang, R. Sun and P. Zhu, A sandwich-structured anisotropic conductive film with robust interfacial reliability and conductivity for functional electrical interconnections, *Chem. Eng. J.*, 2025, **505**, 159721.

22 Q. Liu, Y. Shi, Q. Pan, D. Yang, Y. Lan, Z. Chen and T. Wang, Bioinspired surface engineering of multifunctional tea polyphenols towards ambient fabrication of Cu@ Ni nanowire flexible transparent conductive films, *Appl. Surf. Sci.*, 2025, **715**, 164600.

23 Y. Chen, C. Hao, H. Zhang, W. Xue, S. Cai, C. Jiang, Z. Xiao, G. Cao and Y. Tian, The preparation of polystyrene/nickel core-shell particles for anisotropic conductive films (ACFs), *Prog. Org. Coat.*, 2024, **195**, 108662.

24 P. Rytlewski, P. Augustyn, R. Malinowski, B. Budner and A. Antończak, Surface metallisation of acrylonitrile–butadiene–styrene (ABS) composites *via* a novel electroplating technique, *Appl. Surf. Sci.*, 2025, **712**, 164146.

25 W. Zhang, Y. Zhou, Y. Ding, L. Song, Q. Yuan, W. Zhao, C. Xu, J. Wei, M. Li and H. Ji, Sintering mechanism of size-controllable Cu-Ag core–shell nanoparticles for flexible conductive film with high conductivity, antioxidation, and electrochemical migration resistance, *Appl. Surf. Sci.*, 2022, **586**, 152691.

26 A. Cao, Y. Gong, D. Liu, F. Yang, Y. Fan, Y. Guo, X. Tian and Y. Li, Rapid fabrication of gold microsphere arrays with stable deep-pressing anisotropic conductivity for advanced packaging, *Nat. Commun.*, 2024, **15**, 9182.

27 D. Park, H. Kwak, S. Kim, H. Choi, I. Lim, M. Kwak, I. S. Kim, H. Park, I. Y. Eom, J. W. Lee, I. Park, A. Lee and U. Jeong, Stretchable Anisotropic Conductive Film with Position-Registered Conductive Microparticles Used for Strain-Insensitive Ionic Interfacing in Stretchable Ionic Sensors, *Adv. Funct. Mater.*, 2024, **34**, 2408902.

28 C. Hao, J. Chen, Y. Chen, C. Jiang, Z. Wang, T. Pan, X. Cheng and Y. Tian, Preparation of silver-coated polystyrene microspheres intermediated with polyaniline and their application in array-patterned anisotropic conductive films, *Adv. Compos. Hybrid Mater.*, 2024, **8**, 67.

29 D. Wang, Z. Ma, Z. Han, K. Wu, Y. Liu and X. Tian, Synthesis of high-temperature hydrophobic nanoparticles and their applications in superlyophobic coatings, *J. Mater. Chem. A*, 2025, **13**, 33264–33275.

30 J. S. Arya, M. K. Mahato, S. Sankararaman and E. Prasad, Conducting and superhydrophobic hybrid 2D material from coronene and pyrene, *J. Mater. Chem. C*, 2021, **9**, 10324–10333.

31 X. Yan, B. Ji, L. Feng, X. Wang, D. Yang, K. F. Rabbi, Q. Peng, M. J. Hoque, P. Jin and E. Bello, Particulate–droplet coalescence and self-transport on superhydrophobic surfaces, *ACS Nano*, 2022, **16**, 12910–12921.

32 X. Liu, P. Wang, D. Zhang and X. Chen, Atmospheric corrosion protection performance and mechanism of superhydrophobic surface based on coalescence-induced droplet self-jumping behavior, *ACS Appl. Mater. Interfaces*, 2021, **13**, 25438–25450.

33 Z. Jin, H. Mei, L. Pan, H. Liu and L. Cheng, Superhydrophobic Self-Cleaning Hierarchical Micro-/Nanocomposite

Coating with High Corrosion Resistance and Durability, ACS Sustain, *Chem. Eng.*, 2021, **9**, 4111–4121.

34 S. Wang, Z. Zhao, Q. Yu, P. Li, F. Zhou, C. Xu, X. Zhao and Y. Teng, Superdurable Full-Life Superhydrophobic Composite Block, *Adv. Mater.*, 2024, **36**, e2403853.

35 J. Zhang, Y. Chen, Y. Zhang, S. Wu, J. Sun, X. Liu and J. Song, Fabrication and Energy Collection of Superhydrophobic Ultra-Stretchable Film, *Adv. Funct. Mater.*, 2024, **34**, 2400024.

36 G. Zhang, P. Li, W. Zhao, Y. Wang, L. Zhang, J. Shi, C. Su, W. Du, Z. Li and X. Liu, MXene Nanofluid-Driven Interfacial Synergy for Next-Generation Anisotropic Conductive Films, *ACS Appl. Mater. Interfaces*, 2025, **17**, 55161–55171.

37 G. T. 7124-2008, Determination of tensile lap-shear strength of rigid-to-rigid bonded assemblies, 2008.

38 G. T. 2567-2008, Test methods for properties of resin casting boby, 2008.

39 C. M. Cormican, S. Bektaş, F. J. Martin-Martinez and S. Alexander, Emerging trends in bioinspired superhydrophobic and superoleophobic sustainable surfaces, *Adv. Mater.*, 2025, **37**, 2415961.

40 C. Ye, D. Liu, X. Peng, Y. Jiang, R. Cheng, C. Ning, F. Sheng, Y. Zhang, K. Dong and Z. L. Wang, A hydrophobic self-repairing power textile for effective water droplet energy harvesting, *ACS Nano*, 2021, **15**, 18172–18181.

41 F. Wang, J. Pi, F. Song, R. Feng, C. Xu, X.-L. Wang and Y.-Z. Wang, A superhydrophobic coating to create multi-functional materials with mechanical/chemical/physical robustness, *Chem. Eng. J.*, 2020, **381**, 122539.

